Solar Energy 276 (2024) 112647

Contents lists available at ScienceDirect

Solar Energy

journal homepage: www.elsevier.com/locate/solener

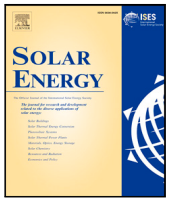

Numerical study of optical transmission in silver plasmonic square nanohole arrays and its application to insulating windows

Jeremy Fleury *, Léo Ferrand, Andreas Schüler

EPFL, Nanotechnology for Solar Energy Conversion Group, Lausanne, Switzerland

ARTICLE INFO

Keywords:
Selective coating
Nano/microstructures
FSS
Plasmonic
Square nanohole arrays
Silver thin film

ABSTRACT

Energy-efficient windows are being used to increase the thermal insulation of a façade. Such insulating windows contain an ultra-thin, multilayered, transparent silver coating that acts as an infrared mirror which significantly reduces thermal losses that occur through radiation from inside the building. These so-called low-emissivity coatings revolutionized the field of building insulation but also decreased solar heat gain coefficient which reduces the potential for energy savings during winter. Insulating windows in cold climates should achieve a selective behavior in the transmittance of EM waves. Ideally, solar energy should be transmitted and mid-infrared radiation reflected, thus reducing the heating needs in buildings. This scientific paper presents a numerical investigation based on finite-difference time-domain (FDTD) focused on the optical transmission characteristics of silver plasmonic square nanohole arrays and explores their potential application in insulating windows. It is found that a nanohole array with a periodicity of 350 nm and a linewidth of 50 nm gives outstanding properties and represents a good candidate to achieve high solar heat gain in low-e coatings. The findings contribute to the understanding of plasmonic effects in nanohole arrays and offer insights into the practical application of such structures in the development of advanced insulating windows with enhanced optical performance.

1. Introduction

Double-pane windows with low emissivity (low-e) coating were developed shortly after the first oil crisis in the early 1970s. It was introduced to the buildings to reduce the energy loss by space heating. Compared to traditional simple glazing, Insulated glass units (IGU) provide a four-time reduction in heat loss, resulting in significant savings. These new windows had a considerable economic impact and have become the industry standard for glazing in industrialized nations. They help offset thermal losses and admit daylight to offset electric lighting [1]. Nowadays, IGUs in cold climates consist of triple glazing with two low-e coatings, but unfortunately, this also means a decrease in total energy transmission within the building. In countries with cold climates, gaining back this solar energy in households could lead to energy savings in space heating. This is why a selective coating could potentially increase the solar heat gain coefficient (SHGC) [2]. One way to achieve this goal is to investigate new approaches [3] such as nano structuration of the coating which allows an increase in solar transmittance (τ_e) and SHGC while maintaining a low thermal emissivity ϵ. Table 1 presents typical values of SHGC and U-values for single, double and triple glazing, with or without a low-e coating.

The ideal selectivity of insulating windows for cold climates (reflection and transmission spectra) is illustrated in Fig. 1. The red and blue lines give the theoretical most effective coating that optimizes the transmission of solar heat gain while minimizing the radiation losses in the mid-IR. This specific selectivity can be achieved by structuring the low-e coating on the windows into a squared nanohole array (inductive-type frequency selective surface (FSS) filter). This mesh-like structure can be described as an inductive filter and acts as a low-pass filter (letting through signal with lower wavelength, i.e. higher frequencies).

As depicted in the literature [4–9], the dimension of the structures is a crucial parameter to achieve optimal selectivity. High transmission in the visible range was demonstrated by structuring silver films into coaxial aperture arrays with a periodicity between 300 and 500 nm. It was also shown that nanohole arrays with a periodicity of 260 nm [10], 300 nm [11] and 600 nm [12,13] in metal films exhibit extraordinary optical transmission. The same physical principles were applied for transmission enhancement of microwaves through periodic slit arrays in metallic films and showed similar results [3,14,15]. Most of the above-mentioned scientific works focus mostly on bio-detection and sensor application. This work will focus on a finite-difference time-domain (FDTD) simulation to investigate the optimal dimensions of

* Corresponding author.
E-mail address: jeremy.fleury@epfl.ch (J. Fleury).

https://doi.org/10.1016/j.solener.2024.112647
Received 14 December 2023; Received in revised form 24 March 2024; Accepted 24 May 2024
Available online 14 June 2024

Table 1
Optical properties of single, double and triple glazing taken from AGC online configurator [16]. For each glazing, the panes consist of a clear-white 4 mm thick float glass and the air gap distance is always 14 mm filled with air. It is compared to the insulated glazing unit with one (or two for triple glazing) iplus 1.0 low-e coating.

	Single		Double		Triple glazing	
	–	Low-e	–	Low-e	–	Low-e
T_v	0.9	0.84	0.82	0.77	0.75	0.65
SHGC	0.88	0.56	0.8	0.51	0.73	0.41
U-Value [W/(m^2 K)]	5.8	3.2	2.8	1.4	1.8	0.8

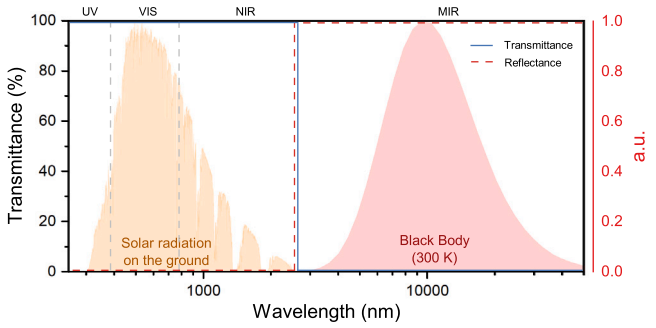

Fig. 1. Transmission and reflection spectra of an ideal solar gain coating. The solar irradiance is transmitted to the building and the radiation from a blackbody at room temperature is reflected to keep the heat inside the room. Both, the global solar irradiance at 1.5 AM and the blackbody radiation are normalized between 0 and 1 and expressed in arbitrary units (a.u.) as reference.

an FSS structure for an application as selective coatings in buildings. First, the theory and structural model used for the FDTD simulation are presented. Its accuracy is then validated by comparing it to the literature. Finally, various design parameters are optimized and an optimal structured coating for high selectivity is presented. To the best of our knowledge, this is the first time that 2D array structures have been optimized to achieve high transmission in the visible spectrum and strong reflectance in the NIR spectrum for building applications.

2. Materials and methods

2.1. Finite-difference time-domain FDTD

To predict the amount of light that is passing through an object, it is needed to understand the interaction between light and matter. This can be achieved by solving Maxwell's equations for EM waves. The four Maxwell's equations are shown as a schematic drawing in Fig. 2 and are shortly explained below:

(1) **Gauss' law:** the divergence of an electric field is proportional to the local density of charge ρ.
(2) **Gauss' magnetism Law:** The divergence of the magnetic flux density is equal to zero, meaning that magnetic monopoles do not exist.
(3) **Faraday's Law:** a time-varying magnetic field induces a spatially varying electric field.
(4) **Ampère's law** (with Maxwell's addition): a variation in time of an electric field or a flowing electric current J will induce a rotational magnetic field.

For isotropic media, the relationship between the electric displacement field D and the electric field E or the magnetic flux density B and the magnetic field H are given as follows:

$$D = \epsilon \cdot E = \epsilon_r \cdot \epsilon_0 \cdot E \quad (1)$$

$$B = \mu \cdot H = \mu_r \cdot \mu_0 \cdot H \quad (2)$$

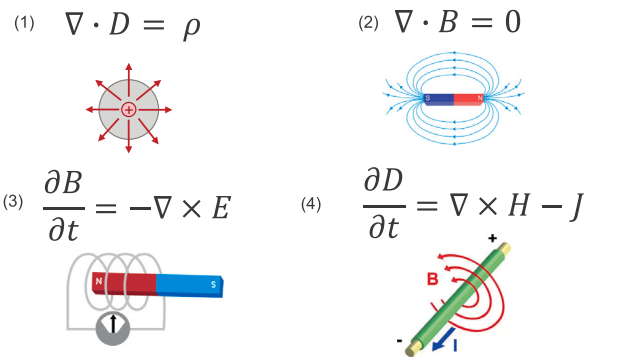

Fig. 2. Illustration of Maxwell's equation in differential form: (**1**) Gauss' Law, (**2**) Gauss' Magnetism Law, (**3**) Faraday's Law and (**4**) Ampere's Law.

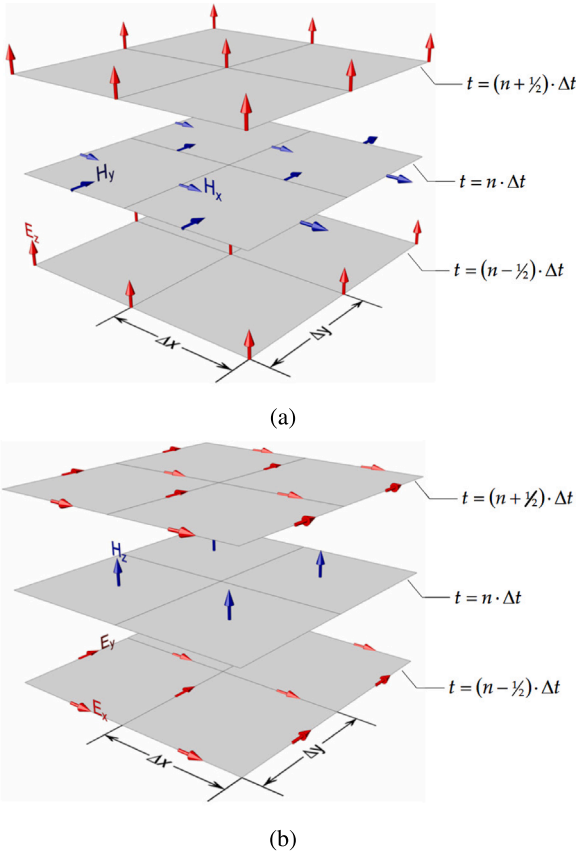

Fig. 3. Visualization of the Yee cell and leapfrog time-stepping for (**a**) TM_z and (**b**) TE_z-mode. A unit cell of Δx by Δy is called a Yee cell. The E_z components are calculated at a distance Δx and Δy, the H components are located in the middle of the cell (in between the E components).

With ϵ being the permittivity (ϵ_0, ϵ_r the vacuum and relative permittivity) and μ the permeability (μ_0, μ_r the vacuum and relative permeability).

Maxwell's equations can be solved numerically using FDTD method. This numerical analysis provides a full-wave solution without any physical approximation and is often used for the simulation of nano-scale optical devices such as nano-patterned metallic films for transparent electrodes [17–19]. As shown in Fig. 3, FDTD (also called Yee's method) consists of using a finite number of grid cells to solve Maxwell's differential equations by approximating derivatives with finite differences. In 2D, these equations can be expressed by the time and spatial

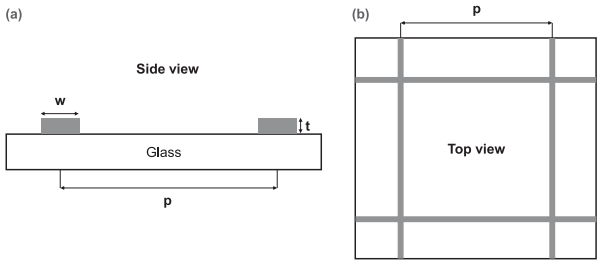

Fig. 4. (**a**) Schematic cross-section and (**b**) top view of a structured coating with w being the width of one line, t the thickness and p the periodicity of one unit cell.

distribution of the E and H field in the corresponding radiation modes TM_z and TE_z:

TM_z-mode

$$\frac{\delta E_z}{\delta t} = \frac{1}{\epsilon}\left[\frac{\delta H_y}{\delta x} - \frac{\delta H_x}{\delta y} - J\right] \tag{3}$$

$$\frac{\delta H_x}{\delta t} = \frac{1}{\mu}\left[\frac{-\delta E_z}{\delta y}\right] \tag{4}$$

$$\frac{\delta H_y}{\delta t} = \frac{1}{\mu}\left[\frac{\delta E_z}{\delta x}\right]$$

TE_z-mode

$$\frac{\delta H_z}{\delta t} = \frac{1}{\mu}\left[\frac{\delta E_x}{\delta y} - \frac{\delta E_y}{\delta x}\right] \tag{5}$$

$$\frac{\delta E_x}{\delta t} = \frac{1}{\epsilon}\left[\frac{\delta H_z}{\delta y} - J\right] \tag{6}$$

$$\frac{\delta E_y}{\delta t} = \frac{1}{\epsilon}\left[\frac{\delta H_z}{\delta x} - J\right]$$

In TM_z-mode (see Fig. 3a), the vertical electric field E_z at $t = (n + 1/2)\Delta t$ is calculated from the spatial distributions of H-field (H_x and H_y) at $t = n\Delta t$ and the initial value of E_z at $t = (n-1/2)\Delta t$. This is depicted by Maxwell's third law shown in Eq. (3). In the next time step ($t = 2n\Delta t$), the H-field is determined from the spatial distribution of E_z and $H_{x,y}$ in the previous time step (Eq. (4)). This finite time-stepping process (leapfrog time-stepping) is repeated as the simulated EM wave travels as a wave package through the structures. An analogous process is carried out for the TE_z-mode presented in Fig. 3b where the simulation starts with a vertical magnetic field H_z.

2.2. Numerical simulation

The optical response in transmission and reflection are simulated on a specially designed High-Performance Computer (32 cores, 256 GB of RAM and high-end 11.2 TFLOPS graphic card (NVIDIA Quadro RTX 5000)) using a commercial software package from ANSYS Lumerical [20]. The general design of the structured coating is presented in Fig. 4, where p stands for the periodicity of the structure, w the width of the lines and t the thickness of the coating. The 3D design of the simulation (Supp. S1) consists of a glass substrate (with a fixed refractive index of 1.52) combined with a thin film of silver with n and k values taken from the literature [21]. An xy-normal incidence plan-wave source is placed above the structure facing downwards to the z-direction (purple arrow). The light is polarized in the x-direction depicting the Transverse electric (TE) mode. Two monitors are placed; one inside the substrate (transmittance) and one behind the source (reflectance). The structured coating is designed as a unit cell combined with periodic boundary conditions in x and y directions to simulate an infinite array of openings. The simulated region is described by the orange box and is composed of perfectly matched layers (PML) at the top and bottom which absorb the EM waves propagating out of the box.

Since the FDTD method solves Maxwell's equations with no approximations, the possible sources of error come only from the numerical error due to the discretization of space and time, the use of artificial PML absorbing boundaries, and the error in the broadband material fit. In this simulation, a mesh size of one-third of the thickness is chosen for high-accuracy simulation of the conductive film. The PML layer is placed far away from the structure and additional absorbing layers are added to reduce possible errors. Finally, the simulation is divided into two wavelength ranges (250–1000 nm and 1000 nm–20000 nm) to improve the fit of the material n and k coefficients.

Optical values, T_v (visible transmittance) and T_e (solar transmittance), are calculated based on Eqs. (7) and (8) [22,23].

$$T_v = \frac{\sum_{\lambda=380\ \mathrm{nm}}^{780\ \mathrm{nm}} D_\lambda T(\lambda) V(\lambda) \Delta\lambda}{\sum_{\lambda=380\ \mathrm{nm}}^{780\ \mathrm{nm}} D_\lambda V(\lambda) \Delta\lambda} \tag{7}$$

where D_λ is the relative spectral distribution of CIE Standard illuminant D65, $T(\lambda)$ the spectral transmittance, $V(\lambda)$ the spectral luminous efficiency for photopic vision and $\Delta\lambda$ the wavelength interval (in nm).

$$T_e = \frac{\sum_{\lambda=380\ \mathrm{nm}}^{2500\ \mathrm{nm}} S_\lambda T(\lambda) \Delta\lambda}{\sum_{\lambda=380\ \mathrm{nm}}^{2500\ \mathrm{nm}} S_\lambda \Delta\lambda} \tag{8}$$

where S_λ is the relative spectral distribution of the global solar radiation AM 1.5 (ASTM G173).

The absorptance can be determined using the conservation law, saying that the addition of the transmittance, reflectance and absorptance is equal to 1. Finally, the emissivity at 300 K is calculated using Eq. (9).

$$\epsilon = \frac{\sum_{\lambda=50\ \mu\mathrm{m}}^{2.5\ \mu\mathrm{m}} BB_{300\ \mathrm{K}} A(\lambda) \Delta\lambda}{\sum_{\lambda=50\ \mu\mathrm{m}}^{2.5\ \mu\mathrm{m}} BB_{300\ \mathrm{K}} \Delta\lambda} \tag{9}$$

with $BB_{300\ \mathrm{K}}$ being the distribution of a black body radiation at 300 K and $A(\lambda) = 1 - T(\lambda) - R(\lambda)$.

3. Results & discussion

3.1. Validation numerical model

The model is first compared with findings based on the light/matter interaction of gold nanohole array as a function of nanohole diameter presented by Q. Tong et al. [24]. As shown in Fig. 5a and b, the side-by-side comparison of the transmittance gives reliable confidence in the model and the simulation code. The gap in peak transmittance for all dimensions can be explained by the different n and k values used for the materials. In the case of d_{hole} = 500 and especially 300 nm, the resonance peaks differ more significantly. This might be explained by the precision of each model: the diffraction effects depend greatly on the mesh size, which in our model was set to 10 nm, but was not mentioned in Q. Tong et al. work. This parameter could explain the discrepancy between the two results for d_{hole} = 300. Moreover, small waves appear in the curves (especially visible for d_{hole} = 900 nm) which may be produced by interference at the boundaries of the unit cell or due to internal reflections within the thick glass layer. Overall, these results confirm that the model created in the simulation software closely describes the behavior of light/matter interaction on structured thin film material.

3.2. Optimization solar radiation vs emissivity

3.2.1. Perfect electrical conductor

A model is first created with a single layer of a perfect electrical conductor (PEC) (infinite electrical conductivity) based on squared geometry presented in Fig. 4. The aim is to investigate the impact on the transmittance of each dimension of the design presented in Fig. 4 (linewidth, thickness and periodicity) in a theoretical approach. Fig. 6a shows the resulting transmittance when the linewidth w is

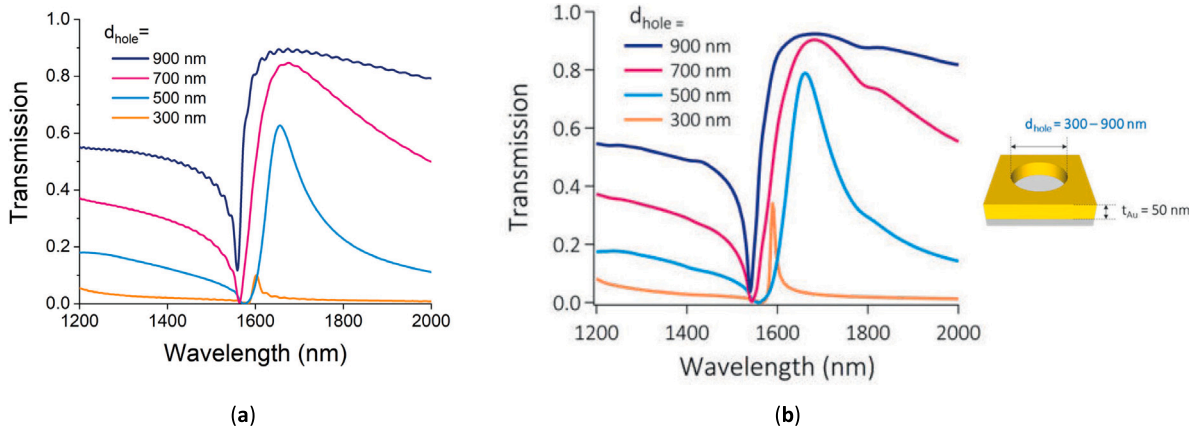

Fig. 5. Simulated transmission spectra of Au nanoholes array as a function of nano-hole diameter. Where (**a**) describes the results from this work and (**b**) simulations based on an article by Q. Tong et al. [24]. The periodicity of the structure is 1000 nm.

varied while the periodicity and thickness are kept constant. As w increases the size of the opening in the mesh diminishes which leads to a reduction in transmittance. The most interesting aspect of this graph is the transmission maximum located around 2,000 nm: for a linewidth of 100 and 200 nm, the peak is first located at exactly 2,000 nm which corresponds to the periodicity of the unit cell. Then, it moves to higher wavelengths as w increases. The 100% transmittance peak is similar to an absentee layer found in thin film interference and metamaterial cloaking [25–27]. For w = 100 nm, high transmittance peaks can also be seen in the visible spectrum, possibly due to the resonance effect.

Larger openings allow higher transmittance, however, the band selectivity is wider. In contrast, smaller openings allow for fewer transmission resonance modes, resulting in sharper peaks and a decrease in the transmission coefficients for wavelengths below the size of the periodicity. When w reaches 1'500 nm, the transmittance falls under 20% meaning that the opening might not be large enough for the successful transmission of light. Fig. 6b presents the influence of the film thickness on the transmittance. All designs exhibit a strong maximum at 100% of transmittance around 2,000 nm. As the thickness increases, this maximum shifts to higher wavelengths and the transmittance cutoff in the NIR spectrum is more pronounced.

Lastly, the periodicity is varied while the p/w ratio is kept at 2.5. The resulting transmittance is shown in Fig. 7. Interestingly, the shape of the curves stays constant throughout all variations. As the periodicity (and hence the linewidth) decreases, the maximum of the peak is blue-shifted. This striking observation means that the transmittance peak could potentially be tuned by modifying the dimension of the structure to achieve high transmittance in visible light and strong reflectance in the NIR. This effect is further investigated in the next section.

3.2.2. Silver squared nanohole array

The final design examined consists of a structured thin Silver film placed on a glass substrate. In this approach, the linewidth-to-thickness ratio is kept at a maximum of 1:1 to comply with manufacturing limitations. Fig. 8 presents the transmittance, reflectance and absorptance spectrum of a 10 nm silver coating and agrees with values reported in the literature [28,29]. The graph can be divided into three parts:

(i) below 322 nm the refractive index is high, meaning that a strong reflection occurs

(ii) around 322 nm, both n and k coefficients are low and the transmittance depends on the skin depth: for an ultra-thin silver film (10 nm) the thickness of the coating lies below the skin depth, meaning that part of the electromagnetic field will propagate through the metal film.

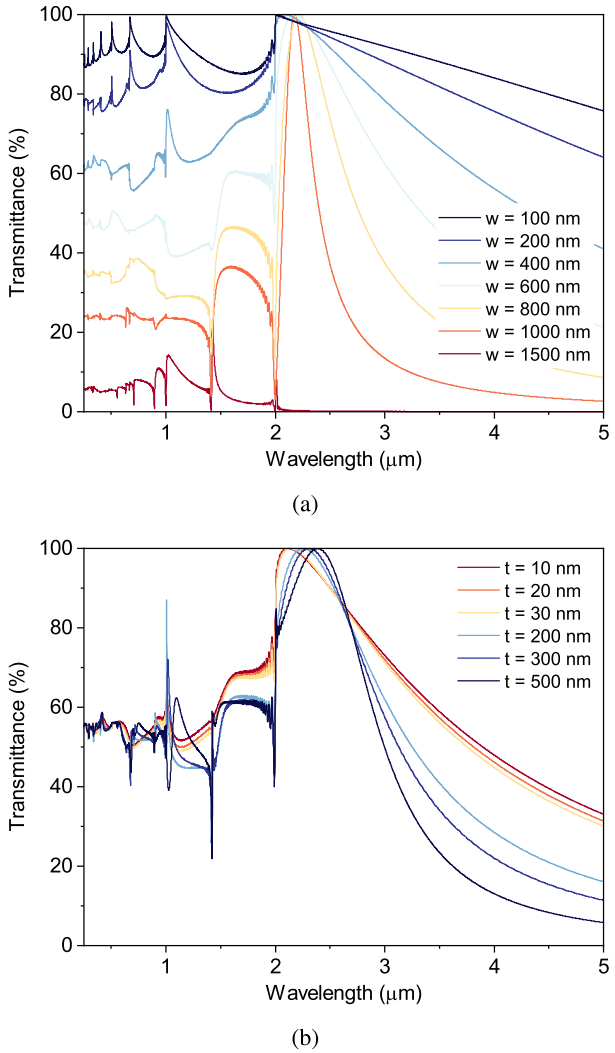

Fig. 6. Transmittance spectra of a structured PEC mesh with a square geometry and a constant periodicity p = 2000 nm. (**a**) the linewidth w is varied from 100 to 1500 nm (t = 35 nm) and (**b**) the thickness t is swept between 10 and 500 nm (w = 500 nm).

(iii) above the plasma oscillation (natural frequency of oscillation within the metal at which free electrons and positive ions may be thought of as plasma) which, for Ag, is located at 322 nm

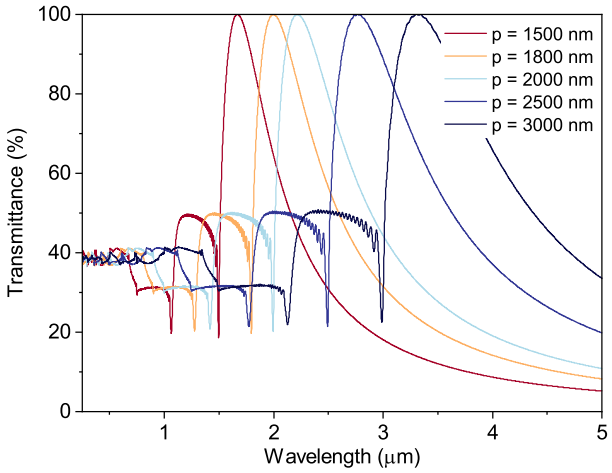

Fig. 7. Transmittance spectra of a structured PEC mesh with a ratio p/w = 2.5 kept constant and a thickness of 35 nm. p is varied and w is adapted accordingly to keep the fixed ratio. The transmission peak moves according to the periodicity.

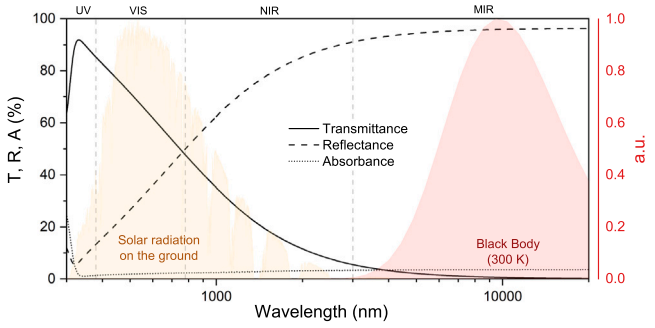

Fig. 8. Transmittance, reflectance and absorptance spectra of a 10 nm Ag coating.

(3.85 eV) [30], the coefficient k is raising drastically leading to an increase in reflection.

As shown in Fig. 9, two different thicknesses of ultrathin Ag film (10 and 50 nm) are compared to a squared nanohole array with a 50 nm thick coating. Because of the larger thickness in the 50 nm thin film, the transmittance is smaller and the cutoff above the plasma oscillation is more defined.

The optimized nanohole array shown in blue has a periodicity, linewidth and thickness of, respectively, 350, 50 and 50 nm. It can be seen that the design exhibits high transmittance in the visible spectrum which then significantly decreases in the MIR range. As mentioned before, the periodicity of the array plays an important role in explaining the transmission peak around 540 nm. Above this wavelength, the EM waves become too large to be transmitted through the mesh-like structure and are mostly reflected. This means that the MIR radiation of a blackbody at room temperature (300K) is reflected, leading to a low emissivity.

Full-wave simulations present the E-field distributions and help understand the behavior of the light when the size of the structure and the wavelengths become similar. Fig. 10 shows the E-field distribution at wavelengths of 363 and 540 nm. At 363 nm, the light is strongly attenuated with a dip in transmittance. It can be seen clearly in the cross-section image (see Fig. 10c) where the electric field increases to more than 13 V/m and shows strong resonance effects on the surface of the film. These plasmon oscillations arise from the interaction of electromagnetic fields with conduction electrons in a metal, propagating along its surface. These propagating surface plasmons, termed surface plasmon polaritons (SPPs), can surpass the conventional

Table 2
Visible, solar transmittance and emissivity. The value for single glazing are taken from AGC [16].

Design	T_v[%]	T_e[%]	ϵ[%]	T_e/ϵ
10 nm Ag	65.8	53.2	3.5	15.2
50 nm Ag	2.9	3.1	1	3.1
Ag nanohole	91.1	78.7	4.7	16.7
Ag nanohole - 4%	87.1	74.7	4.7	15.9
Single glazing with low-e	84	54	~ 3.5	15.4

diffraction limit, influencing light propagation on a subwavelength scale [31]. When periodic holes are introduced into a metal structure, these SPPs enhance light transmission [32]. Additionally, localized surface plasmon resonances (LSPRs) resulting from individual resonances of plasmonic nanoparticles or apertures contribute to the extraordinary optical transmission (EOT) phenomenon [33]. As shown in Fig. 10b, the coupling between SPPs and LSPRs leads to remarkable optical behaviors, such as EOT [34–37]. The EOT behavior is highly dependent on shapes, sizes, hole arrangements, and dielectrics [38,39], providing an opportunity to design innovative plasmonic nanostructures for manipulating light at the nanoscale.

As presented in Table 2, the selective behavior of the nanohole array results in excellent visible and solar transmittance while achieving low emissivity at room temperature. As mentioned by A. Faist [40], a ratio U-value/SHGC allows one to evaluate the thermal quality of glazing: this quality improves when the ratio decreases. In the case of these simulations, the factor ϵ plays an important role in the determination of the U-value and T_e of the SHGC. Hence, the ratio T_e/ϵ should be as high as possible to improve the thermal quality of a glazing.

It should be noted that the low-e coating used in the single glazing consists of a silver thin film combined with additional anti-reflective layer systems which increases the visible and solar transmittance. Finally, to equally compare the low-e with the simulation an additional 4% reflection due to the second glass/air interface (which is not simulated) should be subtracted from the transmittance. Overall, the optimized design achieves an improved visible transmittance and an increase of around 20% points in solar transmittance compared to conventional low-e coating while maintaining low emissivity.

These findings could significantly reduce the heat energy needed in the winter months by optimizing the passive usage of solar energy. The understanding of selective structured coating is also crucial for different applications such as solar cells and high-efficiency greenhouses.

4. Conclusion

The potential of improving the spectral selectivity of thin film by 2D structuring has been investigated. A numerical model is used to simulate the interaction of an incident beam of light on a thin metal coating. The amount of light passing through the film is then monitored by measuring the E-field distributions, which, in turn, gives the transmittance. The model is first validated by comparing it to other simulations found in the literature. It is then used to optimize the size of a silver plasmonic square nanohole array to achieve high transmittance in the visible range and strong reflectance in the MIR (low-e). It is found that a mesh size of p = 350 and w = 50 nm gives outstanding properties and represents a good candidate to achieve high solar heat gain in low-e coatings. This study opens the pathway to the future production of nano-structured samples using, for example, e-beam lithography in a clean room to achieve the required definition in the nano-scale.

CRediT authorship contribution statement

Jeremy Fleury: Conceptualization, Data curation, Formal analysis, Investigation, Methodology, Software, Validation, Visualization, Writing – original draft, Writing – review & editing. **Léo Ferrand:** Data curation, Investigation, Visualization. **Andreas Schüler:** Conceptualization, Funding acquisition, Methodology, Project administration, Resources, Supervision, Writing – review & editing.

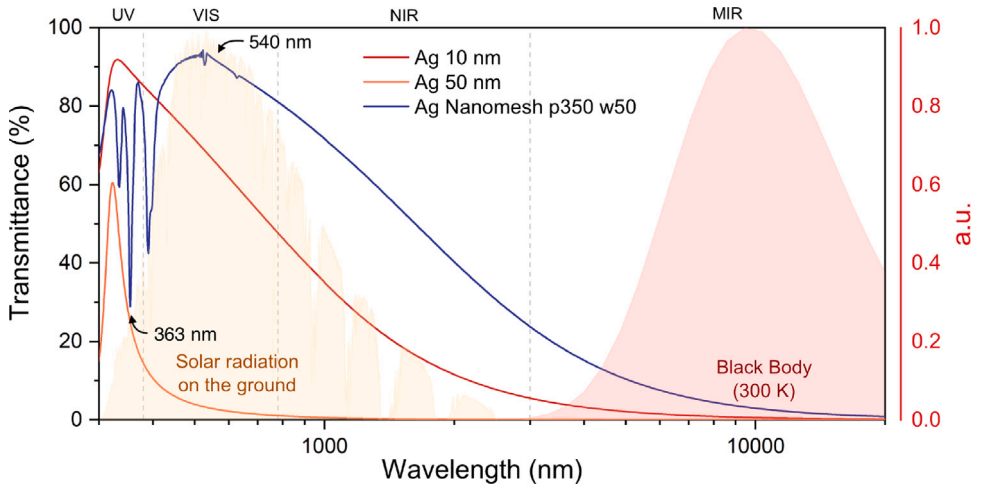

Fig. 9. Transmittance spectra of two Ag coatings with thicknesses of 10 and 50 nm and a silver squared nanohole array film with p = 350 nm, w = 50 nm and t = 50 nm. The structured coating shows high transmittance in the visible range and decreases significantly in the MIR region. Both, the global solar irradiance at 1.5 AM and the blackbody radiation are normalized between 0 and 1 and expressed in arbitrary units (a.u.) as reference.

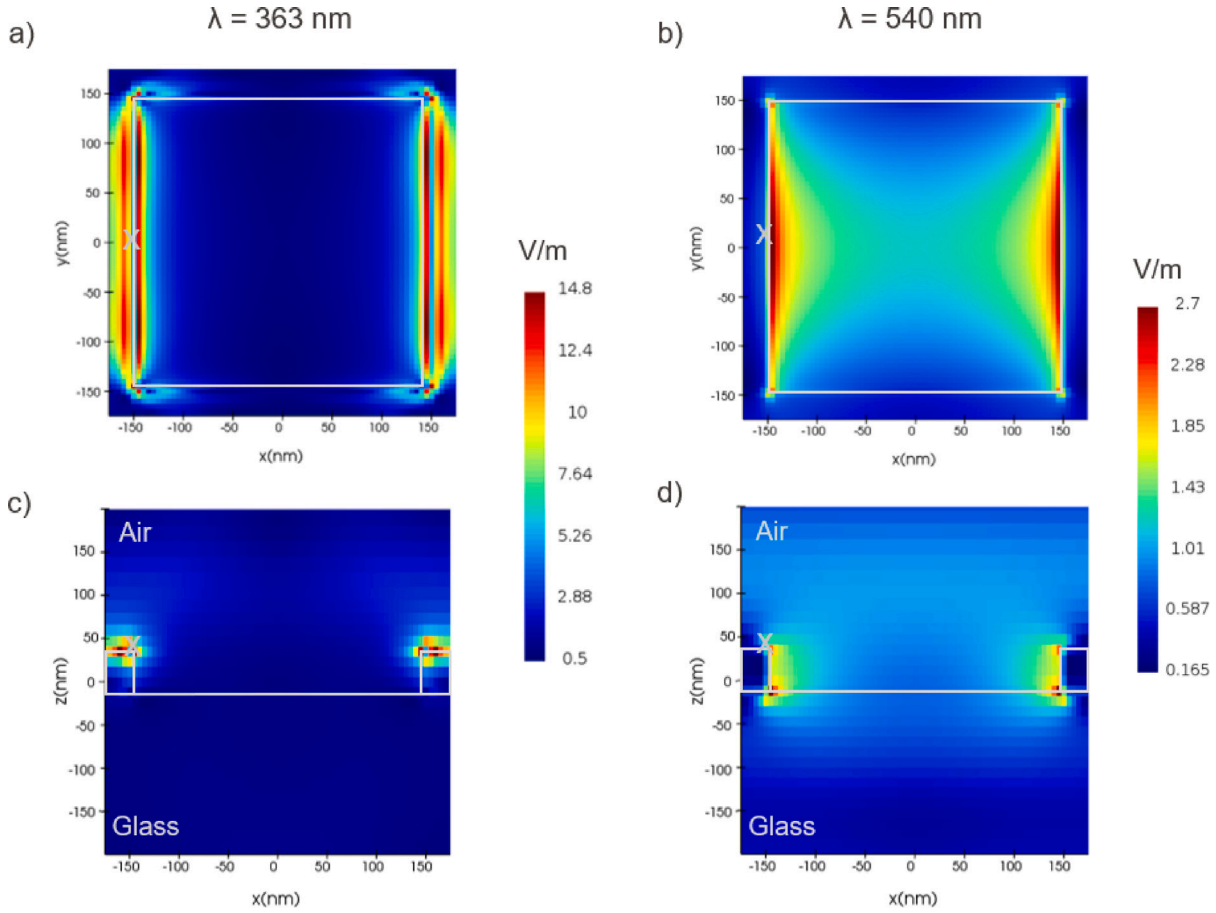

Fig. 10. (**a, b**) Top-view and (**c, d**) cross-section of the electric field distribution in V/m through the mesh at a wavelength of 363 and 540 nm. The edges of the Ag structure are drawn in white lines. The white crosses indicate the location of the monitors.

Declaration of competing interest

The authors declare that they have no known competing financial interests or personal relationships that could have appeared to influence the work reported in this paper.

Data availability

The data that support the findings of this study are available from the corresponding author upon reasonable request.

Acknowledgement

The authors are grateful to Anna Fontcuberta i Morral for the scientific discussion that inspired the simulation aspect of this project and her expertise and support throughout the work.

This research did not receive any specific grant from funding agencies in the public, commercial, or not-for-profit sectors.

References

[1] E. Lee, Lawrence, Handbook of Energy Efficiency in Buildings Chapter 6, in: Innovative Glazing Materials, vol. 3, 2019, https://paper/Handbook-of-Energy-Efficiency-in-Buildings-Chapter-Lee-Lawrence/6a688825134795bca12bc10c8eb03b589ff0f11d.
[2] S. Daqiqeh Rezaei, S. Shannigrahi, S. Ramakrishna, Sol. Energy Mater. Sol. Cells 159 (2017) 26–51.
[3] M. Meier, Mikrostukturierte Metallschichten Auf Glas (Ph.D. thesis), Bayerischen Julius-Maximilians-Universität Würzburg, 2006.
[4] Y. Poujet, J. Salvi, R. Salut, F. Baida, D.V. Labeke, A. Perentes, C. Santschi, P. Hoffmann, Enhanced Transmission of Light through Coaxial Nano-Structures in a Silver Film: Theory and First Experimental Results, in: Nanophotonics, vol. 6195, SPIE, 2006, pp. 396–403.
[5] A.A. Yanik, X. Wang, S. Erramilli, H. Altug, Localized Plasmonic Control of Extraordinary Light Transmission in Rectangular Coaxial Aperture Arrays at Mid-IR, in: Photonic and Phononic Crystal Materials and Devices IX, vol. 7223, SPIE, 2009, pp. 135–142.
[6] Y. Poujet, J. Salvi, F.I. Baida, Opt. Lett. (ISSN: 1539-4794) 32 (20) (2007) 2942–2944.
[7] J. Wang, W. Zhou, E.-P. Li, Opt. Express (ISSN: 1094-4087) 17 (22) (2009) 20349–20354.
[8] X. Jiang, E.S.P. Leong, Y.J. Liu, G. Si, Mater. Des. (ISSN: 0264-1275) 96 (2016) 64–67.
[9] F.I. Baida, Y. Poujet, J. Salvi, D.V. Labeke, B. Guizal, Optics Communications (ISSN: 0030-4018) 282 (7) (2009) 1463–1466.
[10] R. Shafiq, J. Iqbal, A.D. Khan, A.U. Rehman, Opt. Quantum Electron. (ISSN: 1572-817X) 54 (3) (2022) 156.
[11] Y. Qin, J. He, F. Yang, Z. Zhang, Z. Yuan, M. Wu, Optik (ISSN: 0030-4026) 174 (2018) 684–691.
[12] Y. Ekşioğlu, A.E. Cetin, J. Petráček, Plasmonics (ISSN: 1557-1963) 11 (3) (2016) 851–856.
[13] A.E. Cetin, D. Etezadi, B.C. Galarreta, M.P. Busson, Y. Eksioglu, H. Altug, ACS Photon. 2 (8) (2015) 1167–1174.
[14] M.-W. Kim, T.-T. Kim, J.-E. Kim, H.Y. Park, Opt. Express (ISSN: 1094-4087) 17 (15) (2009) 12315–12322.
[15] L. Liu, H. Chang, T. Xu, Y. Song, C. Zhang, Z.H. Hang, X. Hu, Scientific Reports (ISSN: 2045-2322) 7 (1) (2017) 4840.
[16] 2022. Glass Configurator AGC Europe, https://www.agcyourglass.com/configurator/en. (Accessed on 01 December 2022).
[17] P.B. Catrysse, S. Fan, Nano Lett. (ISSN: 1530-6984) 10 (8) (2010) 2944–2949.
[18] S. Shin, S. Ganorkar, J. Kim, Y.-H. Kim, Y.T. Kim, S.-I. Kim, J. Nanosci. Nanotechnol. (ISSN: 1533-4899) 15 (10) (2015) 7640–7644.
[19] C. Stelling, C.R. Singh, M. Karg, T.A.F. König, M. Thelakkat, M. Retsch, Sci. Rep. (ISSN: 2045-2322) 7 (2017) 42530.
[20] Ansys Lumerical FDTD, Ansys Lumerical FDTD, https://www.ansys.com/products/photonics/fdtd.
[21] M.N. Polyanskiy, 2022, Refractive index database, https://refractiveindex.info. (Accessed on 15 September 2022).
[22] EN410:, 2011, Glass in building - Determination of luminous and solar characteristics of glazing.
[23] B.P. Jelle, Sol. Energy Mater. Sol. Cells (ISSN: 0927-0248) 116 (2013) 291–323.
[24] Q. Tong, Direct Laser Writing of Polymeric and Metallic Nanostructures via Optically Induced Local Thermal Effect (Ph.D. thesis), 2016.
[25] W. Cai, U.K. Chettiar, A.V. Kildishev, V.M. Shalaev, Nature Photonics (ISSN: 1749-4893) 1 (4) (2007) 224–227.
[26] Q.-Q. Meng, X. Zhao, S.-J. Chen, C.-Y. Lin, Y.-C. Ding, Z.-Y. Chen, Chinese Physics B (ISSN: 1674-1056) 26 (12) (2017) 124213.
[27] R. Willey, Field Guide to Optical Thin Films, FG07, SPIE, 2006.
[28] J. Gong, R. Dai, Z. Wang, Z. Zhang, Sci. Rep. (ISSN: 2045-2322) 5 (1) (2015) 9279.
[29] E. Valkonen, B. Karlsson, C.-G. Ribbing, Sol. Energy (ISSN: 0038-092X) 32 (2) (1984) 211–222.
[30] A.J. McAlister, E.A. Stern, Phys. Rev. 132 (4) (1963) 1599–1602.
[31] S.M. Orbons, A. Roberts, Opt. Express (ISSN: 1094-4087) 14 (26) (2006) 12623–12628.
[32] W.L. Barnes, A. Dereux, T.W. Ebbesen, Nature (ISSN: 1476-4687) 424 (6950) (2003) 824–830.
[33] B. Ni, L. Huang, J. Ding, G. Li, X. Chen, W. Lu, Opt. Commun. (ISSN: 0030-4018) 298–299 (2013) 237–241.
[34] X. Zhang, G. Liu, Y. Hu, Z. Liu, Y. Chen, Z. Cai, X. Liu, G. Gu, G. Fu, Plasmonics (ISSN: 1557-1963) 9 (5) (2014) 1149–1153.
[35] S.G. Rodrigo, O. Mahboub, A. Degiron, C. Genet, F.J. García-Vidal, L. Martín-Moreno, T.W. Ebbesen, Opt. Express (ISSN: 1094-4087) 18 (23) (2010) 23691–23697.
[36] J. Parsons, E. Hendry, C.P. Burrows, B. Auguié, J.R. Sambles, W.L. Barnes, Phys. Rev. B 79 (7) (2009) 073412.
[37] Z. Jian, L. Jian-jun, Z. Jun-wu, Plasmonics (ISSN: 1557-1963) 6 (3) (2011) 527–534.
[38] G.V. Naik, V.M. Shalaev, A. Boltasseva, Adv. Mater. (ISSN: 1521-4095) 25 (24) (2013) 3264–3294.
[39] J. Qian, Z. Chen, W. Wang, Y. Li, J. Xu, Q. Sun, Plasmonics (ISSN: 1557-1963) 9 (6) (2014) 1361–1369.
[40] A. Faist, 1988, EPFL Le projet LESO, Synthèse des principaux résultats.